

## Eclipsing Binary Populations across the Northern Galactic Plane from the KISOGP survey

FANGZHOU REN,<sup>1,2</sup> RICHARD DE GRIJS,<sup>3,4,5</sup> HUAWEI ZHANG,<sup>1,2</sup> LICAI DENG,<sup>6</sup> XIAODIAN CHEN,<sup>6</sup> NORIYUKI MATSUNAGA,<sup>7,8</sup>  
CHAO LIU,<sup>6</sup> WEIJIA SUN,<sup>1,2,3,4</sup> HIROYUKI MAEHARA,<sup>9,10</sup> NOBUHARU UKITA,<sup>11</sup> AND NAOTO KOBAYASHI<sup>8,12,13</sup>

<sup>1</sup>*Department of Astronomy, School of Physics, Peking University, Yi He Yuan Lu 5, Hai Dian District, Beijing 100871, People's Republic of China*

<sup>2</sup>*Kavli Institute for Astronomy and Astrophysics, Peking University, Yi He Yuan Lu 5, Hai Dian District, Beijing 100871, People's Republic of China*

<sup>3</sup>*Department of Physics and Astronomy, Macquarie University, Balaclava Road, Sydney, NSW 2109, Australia*

<sup>4</sup>*Research Centre for Astronomy, Astrophysics and Astrophotonics, Macquarie University, Balaclava Road, Sydney, NSW 2109, Australia*

<sup>5</sup>*International Space Science Institute–Beijing, 1 Nanertiao, Zhongguancun, Hai Dian District, Beijing 100190, People's Republic of China*

<sup>6</sup>*CAS Key Laboratory of Optical Astronomy, National Astronomical Observatories, Chinese Academy of Sciences, Beijing 100101, People's Republic of China*

<sup>7</sup>*Department of Astronomy, The University of Tokyo, 7-3-1 Hongo, Bunkyo-ku, Tokyo 113-0033, Japan*

<sup>8</sup>*Laboratory of Infrared High-resolution Spectroscopy (LiH), Koyama Astronomical Observatory, Kyoto Sangyo University, Motoyama, Kamigamo, Kita-ku, Kyoto 603-8555, Japan*

<sup>9</sup>*Okayama Branch Office, Subaru Telescope, National Astronomical Observatory of Japan, NINS, Kamogata, Asakuchi, Okayama, Japan*

<sup>10</sup>*Okayama Observatory, Kyoto University, 3037-5 Honjo, Kamogata, Asakuchi, Okayama 719-0232, Japan*

<sup>11</sup>*Okayama Astrophysical Observatory, National Astronomical Observatory of Japan, 3037-5 Honjo, Kamogata, Asakuchi, Okayama 719-0232, Japan*

<sup>12</sup>*Kiso Observatory, Institute of Astronomy, School of Science, The University of Tokyo, 10762-30 Mitake, Kiso-machi, Kiso-gun, Nagano 397-0101, Japan*

<sup>13</sup>*Institute of Astronomy, Graduate School of Science, The University of Tokyo, 2-21-1 Osawa, Mitaka, Tokyo 181-0015, Japan*

(Received February 4, 2021; Revised February 4, 2021; Accepted February 4, 2021)

Submitted to AJ

### ABSTRACT

We present a catalog of eclipsing binaries in the northern Galactic Plane from the Kiso Wide-Field Camera Intensive Survey of the Galactic Plane (KISOGP). We visually identified 7055 eclipsing binaries spread across  $\sim 330$  square degrees, including 4197 W Ursa Majoris/EW-, 1458  $\beta$  Lyrae/EB-, and 1400 Algol/EA-type eclipsing binaries. For all systems, *I*-band light curves were used to obtain accurate system parameters. We derived the distances and extinction values for the EW-type objects from their period–luminosity relation. We also obtained the structure of the thin disk from the distribution of our sample of eclipsing binary systems, combined with those of high-mass star-forming regions and Cepheid tracers. We found that the thin disk is inhomogeneous in number density as a function of Galactic longitude. Using this new set of distance tracers, we constrain the detailed structure of the thin disk. Finally, we report a global parallax zero-point offset of  $\Delta\pi = -42.1 \pm 1.9$  (stat.)  $\pm 12.9$  (syst.)  $\mu\text{as}$  between our carefully calibrated EW-type eclipsing binary positions and those provided by *Gaia* Early Data Release 3. Implementation of the officially recommended parallax zero-point correction results in a significantly reduced offset. Additionally, we provide a photometric characterization of our EW-type eclipsing binaries that can be applied to further analyses.

Corresponding author: Fangzhou Ren, Huawei Zhang, and Richard de Grijs  
renfz@pku.edu.cn  
zhanghw@pku.edu.cn  
richard.de-grijs@mq.edu.au

*Keywords:* Eclipsing binary stars – W Ursae Majoris variable stars – Distance indicators – Milky Way disk – Catalogs

## 1. INTRODUCTION

Eclipsing binary systems (EBS) exhibit optical variability because of geometric properties rather than intrinsic physical changes. EBS encompass almost all stages of binary evolution, covering timescales as long as 1–10 Gyr. This explains their large numbers in the Galaxy. EBS analysis offers a good opportunity to obtain precise fundamental physical parameters from their system properties by means of photometric and/or spectroscopic observations—including their periods and distances, as well as accurate parameters for their components, like masses and radii (e.g. [Torres et al. 2010](#)). This enables us to study unique aspects of their stellar evolution and stellar activity.

EBS can be divided into three types based on their light curve shapes, i.e., Algol (EA)-,  $\beta$  Lyrae (EB)-, and W Ursae Majoris (EW)-type EBS. The total luminosity of EA-type EBS remains almost constant outside the eclipses. EB types exhibit a continuous change in their total brightness outside eclipses while the depth of the secondary minimum is usually considerably smaller than that of the primary minimum. Meanwhile, EW-type light curves are characterized by a smooth shape with symmetric eclipses, and some evolved systems show sinusoidal-like shapes.

EW-type EBS can also be used as reliable distance indicators within the Milky Way. Since their two components fill the system’s Roche lobes, their overall visual magnitude is related to the system’s orbital period (based on Roche lobe theory), which leads to a well-defined period–luminosity relation (PLR). [Rucinski \(1994\)](#) derived the first calibration of such a PLR based on 18 systems, which they eventually improved to an accuracy of 12% ([Rucinski & Duerbeck 1997](#)). Recently, [Chen et al. \(2018a\)](#) established PLRs in 12 optical to mid-infrared passbands based on Tycho–*Gaia* astrometric solution (TGAS) parallaxes, reaching an improved accuracy of 8%. PLRs provide us with a means to determine the distances to EW-type EBS using only photometric light curves. Therefore, as one of the most numerous types of variable systems, EW-type EBS could be used as important Galactic distance tracers ([Matsunaga et al. 2018](#)).

Observations of EBS have a long history. Many ancient cultures observed eclipsing systems (e.g. [Jetsu et al. 2013](#)). In modern astronomy, early-20th century measurements of both EBS and other variables were usually reported in papers discussing individual objects. After the 1980s, large surveys commenced, including the MAssive Compact Halo Objects (MACHO) survey ([Cook et al. 1995](#)) and the Optical Gravitational Lensing Experiment (OGLE; [Graczyk et al. 2011](#); [Pawlak et al. 2013](#); [Pietrukowicz et al. 2013](#); [Pawlak et al. 2016](#); [Soszyński et al. 2016](#)). The number of known EBS and other types of variable stars hence experienced a period of explosive growth. With the development of wide-field cameras, surveys that constantly monitor the entire accessible sky photometrically became commonplace, e.g. the All Sky Automated Survey (ASAS; [Pojmanski 1997](#); [Paczynski et al. 2006](#)) and the Robotic Optical Transient Search Experiment (ROTSE; [Akerlof et al. 2000](#)), part of the Northern Sky Variability Survey (NSVS; [Akerlof et al. 2000](#); [Woźniak et al. 2004](#); [Hoffman et al. 2008, 2009](#)). In the near-infrared (NIR), the VISTA Variables in the Vía Láctea (VVV) Survey offers a less severely reddened window into EBS projected toward the Galactic Center (e.g. [Minniti et al. 2010](#); [Alonso-García et al. 2015](#)). In addition, some all-sky surveys, such as near-Earth object (NEO) surveys whose primary goal is to detect near-Earth asteroids and comets, are also well suited to discover and characterize variable objects, including EBS. This way, candidates from the Lincoln Near-Earth Asteroid Research (LINEAR; [Palaversa et al. 2013](#)), the Catalina Sky Surveys (CSS; [Drake et al. 2014, 2017](#)), the Asteroid Terrestrial-impact Last Alert System (ATLAS; [Heinze et al. 2018](#)), the All-Sky Automated Survey for Supernovae (ASAS-SN; [Kochanek et al. 2017](#); [Jayasinghe et al. 2018](#)), and the Wide-field Infrared Survey Explorer (WISE; [Chen et al. 2018b](#)) have been identified.

Although the accumulation of EBS has multiplied, many previous surveys have avoided targeting the Galactic plane due to the high extinction there compared with less obscured regions. The few available surveys of the Galactic plane tend to cover only a few degrees in Galactic latitude (e.g. [Haas et al. 2012](#); [Hempel et al. 2014](#)). Measurements of EBS are still lacking in the Galactic disk, particularly in the Galactic Anti-center direction. However, understanding the formation and evolution of the Galactic disk, as well as its structure, is a key open issue, since in principle we can investigate our own Galaxy’s structure in much greater detail than that of any other galaxy, thus providing a benchmark for understanding external galaxies.

In this paper, we have collected the light curves of eclipsing binary candidates from the Kiso Wide-Field Camera (KWFC) Intensive Survey of the Galactic Plane (KISOGP), specifically in the northern Galactic Plane, and classified 7055 EBSs. In Section 2, we discuss our data reduction procedures, the classification pipeline, and several parameter distributions, e.g. of periods, magnitudes, and eclipse depths. We also discuss the quality of our EBS sample’s light

curves. Section 3 focuses on the EW types, outlining our analysis procedure and providing a discussion of their distances and extinction values derived from the PLR, absolute parameters, and the structure of the thin disk mapped by EW-type systems and other tracers (e.g. star-forming regions, Cepheids, etc.). We also discuss the parallax zero-point offset affecting *Gaia* Early Data Release 3 (eDR3) parallaxes derived from our EW-type analysis. Section 4 concludes the paper.

## 2. DATA REDUCTION AND RESULTS

### 2.1. Sample Selection

The catalog was compiled from observations taken as part of the KISOGP survey (Matsunaga 2017), acquired with the KWFC on the Kiso 105 cm Schmidt telescope at Kiso Observatory, Japan. The KWFC has been designed for wide-field observations, taking advantage of the Kiso Schmidt telescope’s large focal-plane area. It mosaics eight CCD chips with  $8k \times 8k$  pixels in total and covers an area of  $2.2^\circ \times 2.2^\circ$ . Typically, for any object, more than 200 exposures were acquired in the  $I$  band to a depth of  $I = 9.5\text{--}17$  mag with a signal-to-noise ratio (S/N) better than 30. The main goal of the survey is to study the Galactic disk using variable stars as tracers (e.g. Miras; Yao et al. 2017). The KISOGP survey covers the northern Galactic disk, which spans from  $60^\circ$  to  $210^\circ$  in Galactic longitude, and from  $-1^\circ$  to  $1^\circ$  in Galactic latitude. The region  $70^\circ < l < 80^\circ, 1^\circ < b < 3^\circ$  is also covered. (For the relevant maps and pointings, see Figure 1 of Matsunaga 2017).

For each epoch, a 5 s exposure and three 60 s exposures are taken to optimally cover the full magnitude range. The 5 s exposure is suitable for stars at the bright end ( $I \sim 9$  mag), while the 60 s exposures are better for the faint end, from  $I = 11$  mag down to  $I = 17$  mag. A reference target list was established by combining all epochs. Candidate variable stars were selected by considering three variability indices, including interquartile ranges, weighted standard deviations, and von Neumann ratios (Sokolovsky et al. 2017). Among  $\sim 8$  million stars whose time-series data were examined, more than 50,000 objects were selected as candidate variable stars (N. Matsunaga et al., in prep.). In this paper, 7752 candidate variables are considered for our EBS selection, based on Fourier analysis, with periods determined in Section 2.2 (Chen et al. 2020).

### 2.2. Eclipsing Binary Selection

To properly identify EBS, high-quality folded light curves are needed. The basic idea is to determine optimally constrained periods of variability. We adopted the Lomb–Scargle (LS) periodogram (Lomb 1976; Scargle 1982) and String–Length (SL) methods (Lafler & Kinman 1965; Clarke 2002) to obtain optimal periods for all candidates.

The input periods ranged from 0.08 to 10 days in steps of 0.00001 days (for the LS method). The short-period limit for known EW types is 0.16 days (Soszyński et al. 2015). Ultra-short-period EW types, which usually contain highly evolved stars, usually exhibit sinusoidal-like light curves. In this situation, the primary and secondary minima may have similar depths. They are often misidentified as the same feature in phased light curves. This will result in an output harmonic or aliased period of the true period, where  $P_{\text{output}}/P_{\text{true}}$  is a ratio of integers, usually 1:2. For this reason, we start at one-half of 0.16 days. Any harmonic period found will be corrected during our subsequent visual determination by multiplying the period to make sure that two eclipses occur within a single period.

To further improve the accuracy of our period determination, the SL method was applied to the output periods from the LS method. We tried 2000 periods within 0.0002 days around the output period. This led to an improvement in the fifth decimal place: the majority of our EBS (64.1%) have periods with errors smaller than  $1 \times 10^{-5}$  days. The output periods will be used as input periods for our visual verification.

### 2.3. Visual Verification

Armed with the periods thus determined, a visual check was done of the photometric parameters and type determination based on phased light curves. EBS candidates were selected based on visual examination of their light-curve morphology. We removed all objects classified as other types of variable stars, such as RR Lyrae, Cepheids, non-periodic variables, etc. Meanwhile, a visual check of the period (particularly for those objects for which we need to multiply the period to encompass two eclipses within a single period), a visual determination of the phase of the primary eclipse (which will be shifted to 0 and represents  $t_0$ ), the system’s magnitude outside the eclipse, and the primary and secondary eclipses were done. Subsequently, the objects’ types were determined.

The order in which we examined the candidates was random, and all objects were processed randomly three times. If a system’s type determination was the same and the standard errors of the parameters were less than 0.02 mag or

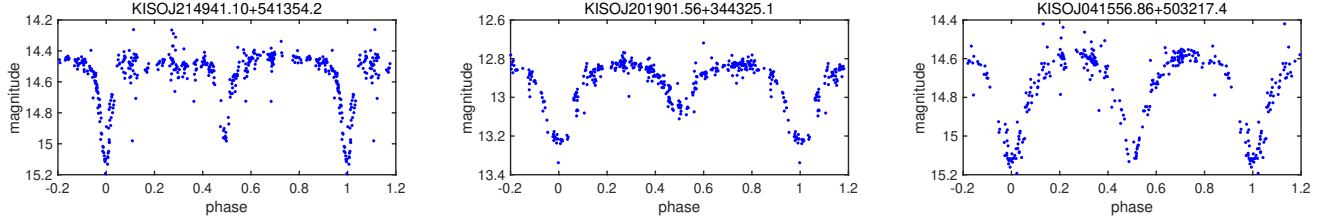


Figure 1. Examples of EA-, EB-, and EW-type EBS (left to right).

Table 1. Eclipsing Binaries Catalog

ID	Exposure	Type	Period	$err_P$	$t_0$	$I_{max}$	$I_{pri}$	$I_{sec}$	Ratio	Distance	$A_V$	$\Delta m_{2MASS}$
			days	$10^{-7}$ days	days	mag	mag	mag				
KISOJ000009.94+612905.2	264	EA	1.4418015	67	56167.64799	13.660	14.039	13.833	0.456	...	...	...
KISOJ000010.73+621848.8	189	EW	0.3890992	38	56167.69297	15.414	15.562	15.538	0.838	2.387	0.860	0.021
KISOJ000017.82+625339.6	184	EB	0.5820739	23	56167.31869	15.552	15.960	15.754	0.495	...	...	...
KISOJ000026.19+632139.0	43	EW	0.3180290	393	56175.60476	16.333	16.856	16.804	0.901	2.298	1.469	0.422
KISOJ000039.63+622214.1	174	EW	0.2859520	1	56167.59347	16.137	16.458	16.390	0.788	1.646	1.778	0.253
KISOJ000048.17+614603.1	178	EW	0.3024461	1	56167.77640	16.016	16.732	16.637	0.867	1.352	2.612	0.705
KISOJ000053.24+613059.8	256	EW	0.2826091	1	56167.60270	16.093	16.441	16.378	0.819	1.747	1.497	0.041
KISOJ000056.84+625228.4	267	EW	0.5717867	12	56167.37203	14.228	14.445	14.440	0.977	1.986	1.657	0.158
KISOJ000111.08+625139.7	113	EB	1.0133044	1	56167.36126	16.160	16.758	16.492	0.555	...	...	...
KISOJ000112.76+623859.7	296	EA	1.3701021	99	56167.30771	14.589	14.835	14.819	0.935	...	...	...
KISOJ000123.66+613746.8	230	EW	0.3871284	8	56167.49329	15.738	16.049	16.004	0.855	3.088	0.401	0.153
KISOJ000132.54+615234.2	78	EW	0.3660444	36	56251.31592	16.772	17.107	17.092	0.955	3.148	1.900	0.177
KISOJ000135.90+624456.3	171	EB	0.7391682	1	56167.17345	16.514	16.946	16.700	0.431	...	...	...
KISOJ000138.55+615348.4	186	EA	0.7856778	147	56167.74912	12.237	12.485	12.405	0.677	...	...	...
KISOJ000145.92+614214.0	265	EB	0.3333018	2	56167.67988	12.087	12.746	12.382	0.448	...	...	...
KISOJ000208.16+630633.5	311	EW	0.3092946	1	56167.58121	12.957	13.164	13.141	0.889	0.577	0.639	0.080
KISOJ000210.22+611924.2	175	EW	0.4997257	21	56167.51962	16.190	16.413	16.371	0.812	3.863	1.878	0.013
KISOJ000233.43+614514.3	167	EW	0.3152875	1	56167.71510	16.774	17.297	17.199	0.813	3.119	1.019	0.060
KISOJ000240.13+622844.5	285	EW	0.4282596	3	56167.75852	14.515	14.622	14.618	0.963	1.645	1.237	0.094
KISOJ000250.76+624850.0	169	EW	0.2579880	407	56175.50704	15.813	16.165	16.162	0.991	1.330	1.441	0.060
...	...	...	...	...	...	...	...	...	...	...	...	...

NOTE—This table is available in its entirety in machine-readable form.

0.02 in phase, the corresponding type and the mean values of the thrice-determined parameters were adopted. For those objects that failed to pass this round, this procedure was repeated.

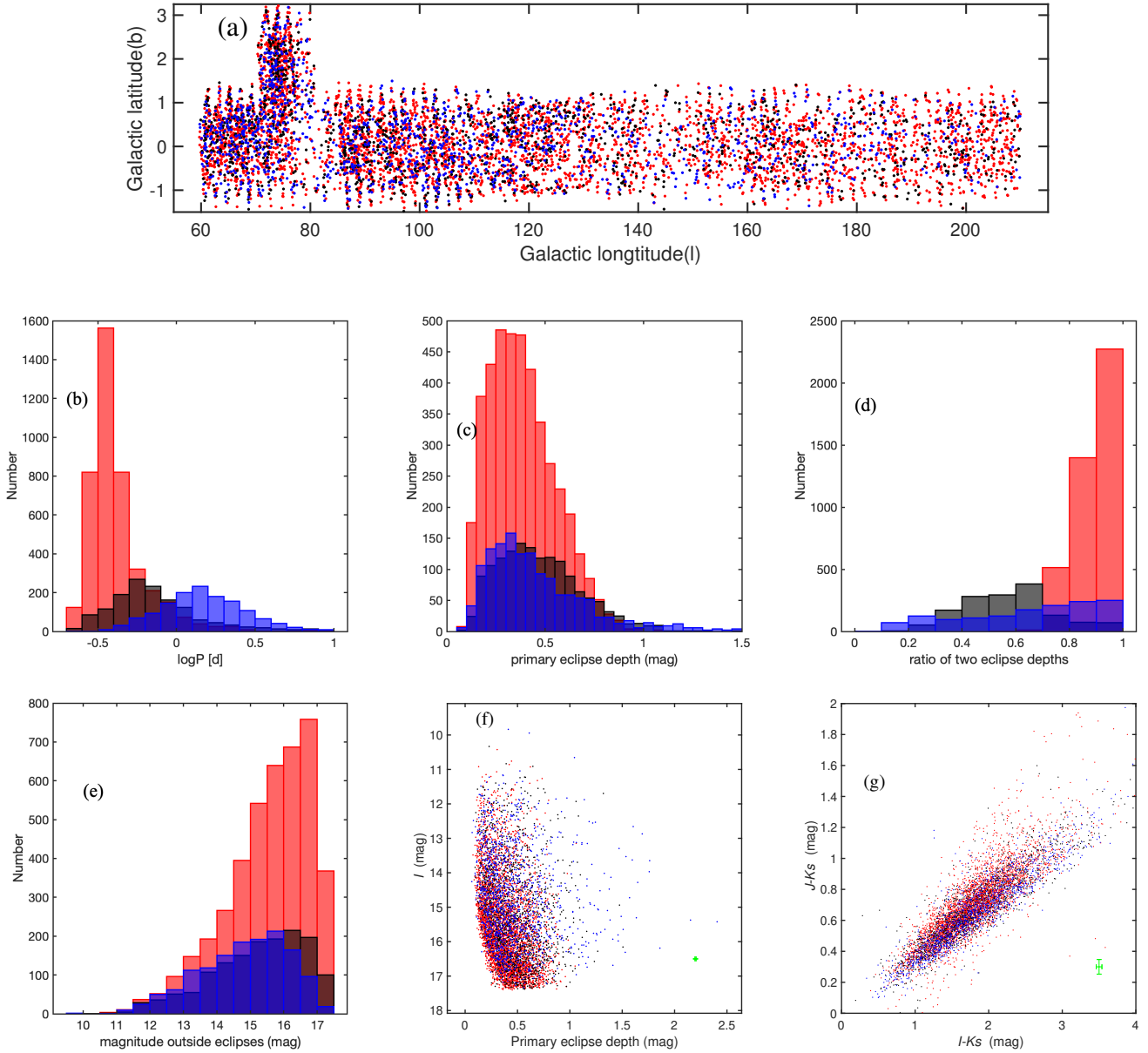
Our final catalog contains 7055 carefully visually selected EBS, composed of 4197 EW-, 1458 EB-, and 1400 EA-type systems. Figure 1 shows three randomly selected sample light curves.

Table 1 includes all EBS parameters, including the system ID, effective number of exposures, coordinates, type, period and period error,  $t_0$  in units of the modified heliocentric Julian date (HJD-2400000.5; which sets the primary eclipse at phase zero), the maximum magnitude outside eclipses, the magnitudes of both eclipses within one period in the  $I$  band, and the depth ratio of the two eclipses. The objects' distances, extinction values in the  $V$  band for EW-type systems, and the magnitude differences in the Two Micron All Sky Survey (2MASS; [Skrutskie et al. 2006](#)) photometric system will be described in Section 3.1.

#### 2.4. Distribution Map

The parameter distributions for all EBS are shown in Figure 2. Red points or bars represent EW types, while black and blue symbols correspond to EB and EA types, respectively.

The EBS distribution as a function of Galactic longitude is shown in Figure 2a. It is inhomogeneous in number density. This inhomogeneity is caused by the presence of groups of stars associated with the Galaxy's spiral arms, including the Orion Spur and the Perseus Arm. Since EBS variability is caused by the systems' geometry, independently



**Figure 2.** EBS distributions. Red, black, and blue points and bars represent the 4197 EW-, 1458 EB-, and 1400 EA-type EBSs, respectively. The green points with error bars in panels (f) and (g) indicate the representative error bars pertaining to all samples in the respective panels. (top) Positions of all EBS in Galactic coordinates (in units of degrees). (middle left) Periods (logarithmic units). (middle center) Primary eclipse depths ( $I$  mag). (middle right) Ratios of secondary to primary eclipses. (bottom left) Magnitudes outside eclipses (total EBS magnitudes in the  $I$  band). (bottom center) Scatter of the total  $I$ -band magnitude over primary eclipse depth for each EBS. (bottom right) Color-color diagram ( $I - K_s$  vs  $J - K_s$ ; with  $J$  and  $K_s$  magnitudes from 2MASS).

of any other criteria associated with object position or selection bias, the EBS distribution is representative of the general distribution of stars in the Galaxy (Rucinski 2006). Extinction also plays an important role in the observed inhomogeneity, since dust obscuration and scattering have a significant effect on stars in the Galactic plane. Only nearby stars can be seen projected toward the most obscured regions. We will return to the inhomogeneous distribution of EBS in Section 3.2.

There are obvious period differences among the three types of EBS in Figure 2b. EA types have the longest periods, ranging from 0.3 to 10 days, with a peak at several days. EW types have the shortest periods, i.e., shorter than one

day; most EW types have periods around 0.3–0.5 days. Both the period range and the peak period of EB types are found in the middle of the three types. Their period distribution also depends on their environment. EBS in the Galactic plane are thought to be less evolved and have longer periods than those outside the thin disk, since they are usually younger. This is shown in the left panel of Figure 3; see Section 2.5 for a discussion.

For EA types, extremely wide period ranges have been reported in the literature (e.g. Graczyk et al. 2011), reaching up to thousands of days. Our detection approach prevents us from detecting such long-period variables. We are constrained to a longest period of 50.22 days. For EA types with longer periods, it will be harder to fully cover the eclipses to identify their types. However, instead of continuous monitoring, only a few epochs are taken during a given night for each object in our survey, which makes it harder to completely cover their full eclipses. Some EA-type candidates with extremely long periods may only have a few detections during their eclipses. The numbers of detections may be insufficient to characterize such an eclipse, and so such samples would fail to pass our selection criteria. Therefore, our catalog lacks long-period EA-type EBS.

No clear differences in the distribution of the primary depths can be seen, but the distribution of the eclipse-depth ratios varies significantly among the different EBS types (see Figure 2c-d). A clear plateau can be seen in the histogram of the eclipse-depth ratios of EA-type EBS between 0.1 and 1. Secondary eclipses may not be visible if the stars are considerably different in size. It is impossible to distinguish EA types with an invisible secondary eclipse from EBS featuring a double period characterized by similar eclipses solely based on light curves. This may be the reason for the lack of a plateau at the shorter end of the eclipse-depth distribution. Nevertheless, the observed distribution underscores that the EA-type eclipse-depth ratios are randomly distributed, while the ratio of EW types is close to unity, as expected.

The histogram of the magnitudes outside eclipses, the scatter in magnitude during the eclipses, and a color–color diagram exhibiting a roughly linear relation for all types of EBS are shown in Figure 2e-g. The lack of faint EBS with shallow eclipses is caused by selection effects. Faint systems with shallow eclipses, whose magnitude errors during every single epoch are comparable to the eclipse depth, would not pass our selection procedure.

### 2.5. Possible Contamination by Other Variables

We selected our EBS sample using the same method as that proposed by Chen et al. (2020). Contamination of our sample by non-binary objects is less than 1%, based on careful visual examination. Since different types of variables exhibit different kinds of light curves, it is easy to distinguish EA- and EB-type EBS from other types of variables, even without access to any color information. RRc Lyrae and EW-type EBS have similar periods and amplitudes. An RRc Lyrae light curve with a nearly symmetric luminosity decrease may be misclassified as an EW-type EBS characterized by two similar-depth eclipses at double the RR Lyrae’s period. As such, RRc Lyrae are the main possible contaminant. Here we evaluate the likely level of this type of contamination.

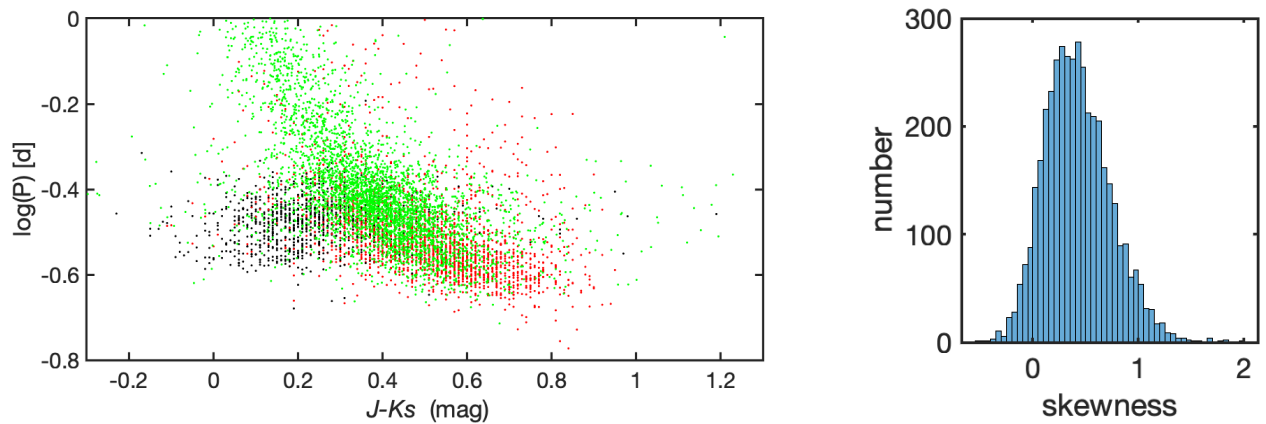


**Figure 3.** Assessment of the possible contamination caused by RRc Lyrae. (left) EW-type color–period distribution. Green: Our EW-type sample objects; black and red: RRc Lyrae and EW-type systems, respectively, from Palaversa et al. (2013). (right) Skewness distribution of our sample.

This degeneracy can be lifted by considering the light-curve skewness and color. EW-type objects are associated with a significantly larger skewness than RRc Lyrae. The latter exhibit more sinusoidal-like light curves, while EW-type variables remain brighter for longer during their out-of-eclipse phase. EW-type objects are also significantly redder. These properties will be helpful in aiding our efforts to prevent contamination of our EW-type sample by RRc Lyrae (see, e.g. Palaversa et al. 2013).

Figure 3 presents the color–period and skewness distributions of the EBS discussed in this paper. In the left panel, we show the de-reddened 2MASS  $J - K_s$  colors as green points (the extinction values were taken from Section 3.1), as well as the LINEAR RRc Lyrae and EW types (black and red points, respectively). Since all LINEAR objects are located at high Galactic latitude ( $b > 29^\circ$ ), their extinction values are negligible in  $J - K_s$ . Among our LINEAR objects, RRc Lyrae are generally bluer than EW-type EBS. Our EW-type sample objects are scattered from the top to the right section of the color–period plane, where we see little contamination by RRc Lyrae; they match the LINEAR EW types well. The skewness distribution is shown in the right panel. The adopted boundaries of the skewness, based on the LINEAR sample, are  $-0.1$  to  $1.6$  for EB/EW types and  $-0.4$  to  $0.35$  for RRc Lyrae. Our sample’s distribution matches that of the LINEAR sample quite well.

Although it is hard to exclude all RRc Lyrae solely based on our current photometric data, contamination effects appear negligible according to these color and skewness tests.

### 3. DISCUSSION OF OUR EW-TYPE SAMPLE OBJECTS

#### 3.1. Extinction and Distance

Lucy (1968a,b) proposed convective common-envelope evolution as the key idea underlying EW-type theory. The modern model (Stepień 2006a; Yildiz & Doğan 2013) suggests that EW types form through both angular-momentum loss and nuclear evolution. EW types are in their late stage of evolution, and it has been shown observationally that both components have similar temperatures. EW-type binaries usually form a common envelope and they can thus be regarded as a single structure. In the color–magnitude diagram, they appear as objects close to the main sequence (MS), although one or both components may be more advanced in their evolution (Stepień 2006a,b, 2009, 2011). Among stars in the Galactic disk, EW-type objects are usually found in old open clusters. Meanwhile, as one of the most numerous types of variables in the Galactic field, they can potentially be used to determine the Galactic disk’s structure above and below the Galactic plane and to trace any age gradient across the plane (Chen et al. 2018a). However, studies of the distribution of EW-type systems in the Galactic plane are limited. With our sample, we can now partially fill in the blanks.

Since the publication of Eggen (1967), a number of attempts have been made to use EW-type period–luminosity–color relations as potential distance indicators. Rucinski made several attempts to derive PLRs from nearby EW types (Rucinski 1994), EW types with *Hipparcos* parallaxes (Rucinski & Duerbeck 1997), ASAS catalogs (Rucinski 2006), and TGAS parallaxes (Mateo & Rucinski 2017). To unify the PLRs obtained from different bands, optical-to-mid-infrared PLRs from Chen et al. (2018a), based on 183 nearby EW-type systems with TGAS parallaxes, were adopted.

Note that our sample objects are located in the Galactic disk, where the extinction is high and varies significantly. Although the KISOGP survey can efficiently reduce the impact of extinction in the  $I$  band compared with that in  $V$  band, extinction is expected to still have a sizeable effect on the resulting photometry.

To derive accurate distances, we considered distance moduli ( $\mu_0$ ) and extinction values ( $A_\lambda$  as a function of passband,  $\lambda$ ) as variable parameters, i.e.

$$m_\lambda - a_\lambda \times \log P - b_\lambda = (A_\lambda/A_V) \times A_V + \mu_0. \quad (1)$$

For a given passband  $\lambda$ , we take the PLR coefficients  $a_\lambda$  and  $b_\lambda$  from the maximum-magnitude coefficients of the PLRs of Chen et al. (2018a); the extinction law,  $A_\lambda/A_V$ , from Wang & Chen (2019); and the period,  $\log P$ , from Table 1 in Section 2.3. For the apparent magnitude,  $m_\lambda$ , we adopt the maximum  $I$ -band magnitudes from Table 1, combined with  $JHK_s$ -band data from 2MASS. However, 2MASS only provides single-epoch photometry, as well as a time stamp for the observation. Since observed color changes are very small during eclipses, the light-curve shape barely changes among the different bands (Chen et al. 2016). This makes it possible to convert the single-epoch magnitudes to the corresponding maximum magnitudes obtained from the full  $I$ -band light curves. The differences between the  $I$ -band magnitudes in the observational phase and the maximum  $I$ -band magnitudes are listed in Table 1. These photometric properties also allow us to convert the 2MASS single-epoch photometry to the maximum  $JHK_s$ -band magnitudes.

Armed with known or newly determined parameters pertaining to the  $IJK_s$  bands, it is now possible to fit the  $(\mu_0, A_V)$  combination for each system; for an example, see Figure 4. A similar method has been adopted by other authors (e.g. Madore et al. 2017).

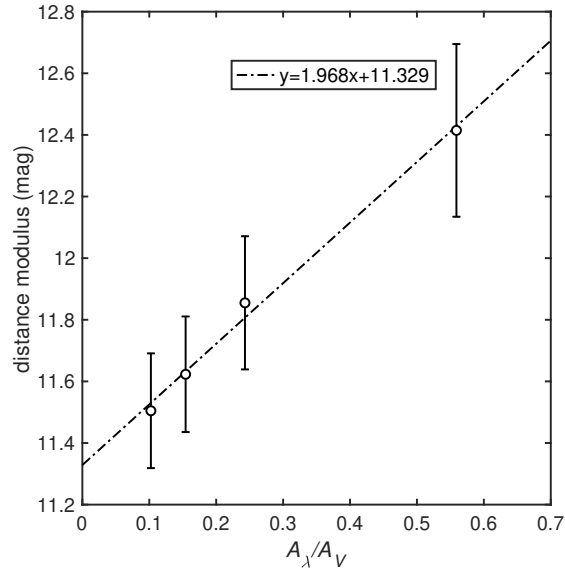


**Figure 4.** Example of our determination of extinction and distance. The intercept corresponds to the distance modulus,  $\mu_0 = 11.329$  mag, while the slope reflects the extinction in the  $V$  band,  $A_V = 1.968$  mag.

In this example, the slope corresponds to the  $V$ -band extinction,  $A_V$ , and the intercept is the best-fitting distance modulus,  $\mu_0$ . Since the PLR was fitted only to EW-type objects, our results are based on 3996 objects, having first excluded systems without 2MASS observations. The best-fitting distances and extinction values are listed in Table 1. For some sources affected by low extinction, negative slopes implying negative extinction may result for numerical reasons; in those cases we set the extinction to zero.

As an independent means to determine distances, EW-type PLRs have a wide variety of uses, including as a probes to map the structure of the Galactic plane and as benchmarks to crosscheck other means of distance determination.

### 3.2. Mapping the Galactic Thin Disk Structure with EW types

Equipped with distance estimates from our PLR application, it is now feasible to derive the structure of the northern Galactic plane as traced by EW-type EBS. To minimize selection effects, we excluded KISOGP objects located at  $70^\circ < l < 80^\circ, 1^\circ < b < 3^\circ$  to retain a uniform distribution across  $-1^\circ < b < 1^\circ$  of the thin disk.

The spatial and extinction distributions of EW-type tracers derived from application of the PLR are shown in the top panel of Figure 5. Different colors represent different extinction values; all objects affected by  $A_V \geq 5$  mag have been assigned the same color. Our sample objects near the Sun are, in general, affected by low extinction, usually less than  $A_V = 2$  mag, while objects in more distant regions are significantly more highly obscured. The spatial distributions defined by different tracers, as well as that traced by our EW types, are shown in the bottom panel of Figure 5. Members of high-mass star-forming regions (HMSFRs; Reid et al. 2014), Galactic Cepheids (Genovali et al. 2014), and the 478 EA- and 454 EB-type objects from Table 1 with accurate *Gaia* parallaxes ( $0 < \sigma_\pi/\pi < 0.1$ ) are shown as magenta diamonds, red circles, and cyan and black triangles, respectively. EW-type systems with distances obtained from the PLR are also shown in the density map. The density map was constructed using MathWorks’ ‘scatplot’ tool<sup>1</sup>, while colored data points and contours were plotted using Voronoi cells to determine the relevant densities. Members of all groups are dispersed in the same region across the northern Galactic thin disk.

The density distributions of EW-type and other tracers show that the Galactic thin disk appears inhomogeneous. This exercise can potentially help us to reveal substructures such as bubbles and filaments. Meanwhile, the components

<sup>1</sup> <https://www.mathworks.com/matlabcentral/fileexchange/8577-scatplot>



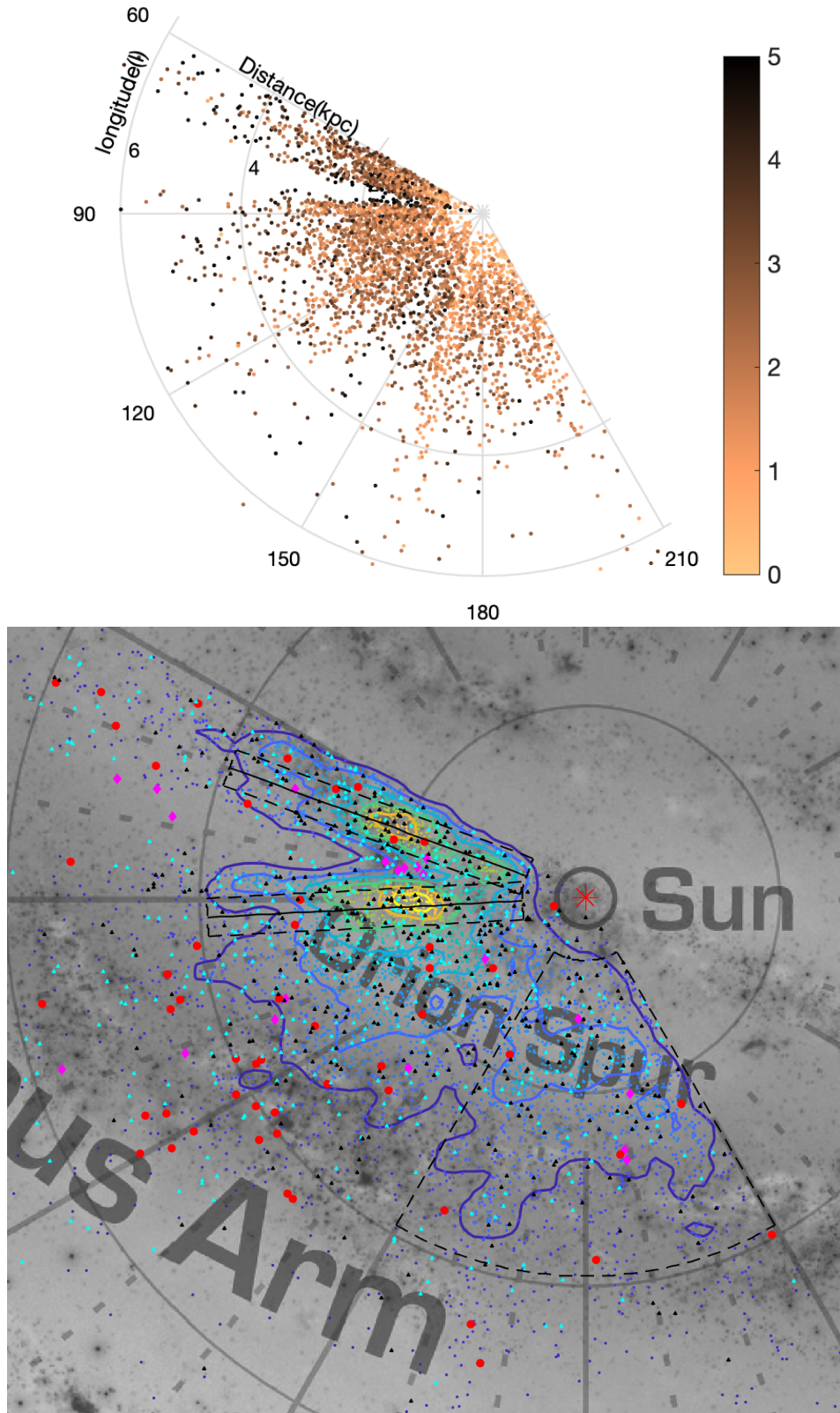


**Figure 5.** Spatial distribution of EW-type EBS in the Galactic thin disk. (top) Space and extinction distributions looking down on the Milky Way, centered on the Sun. Different colors represent different extinction values as reflected by the color bar. (bottom) Spatial distribution of the EW-type EBS as seen from the Galactic North Pole. A density map of our EW types is shown as contours (from blue to yellow). The Sun is shown as a red star symbol. Some other tracers are also included for comparison. High-mass star-forming regions (Reid et al. 2014) are shown as magenta diamonds, Galactic Cepheids (Genovali et al. 2014) are shown as red circles, while EA- and EB-type EBS from Table 1 with accurate *Gaia* parallaxes ( $0 < \sigma_\pi/\pi < 0.1$ ) are shown as cyan and black triangles, respectively. Members of all groups are dispersed across the northern Galactic thin disk in the same region. Background image credit: Modified from the original artist’s conception; NASA/Joint Propulsion Laboratory–California Institute of Technology/R. Hurt (Spitzer Science Center).

of EBS usually form from MS stars, and their differences within each type of EBS are not affected by age (or at most to a limited extent). Different EBS types are generally associated with different ages, in the sense that EA types are younger, EB types are older, and EW types are the oldest tracers. Meanwhile, Cepheids are young stars and HMSFRs are very young. These different tracers can thus also be used as age tracers.

The derived structure of the thin disk varies significantly as a function of direction. In some directions, e.g. toward  $l \sim 120^\circ$  and  $l \sim 165^\circ$ , EW types can be seen out to considerable distances given the slowly increasing extinction trends there. It appears that these directions offer low-extinction windows, reaching and even crossing the Perseus Arm. These areas are known as diffuse regions (Wang et al. 2017, their Figure 1). In other directions, the extinction increases quickly and the largest visible distance from the Sun is small. For example, around  $l \sim 80^\circ$  a clear lack of objects is caused by high extinction,  $A_V > 5$  mag within 1 kpc. A young, dense cloud with high star-forming activity and high extinction is located in that direction (i.e., the Cygnus X region; Rygl et al. 2012). Its location among the accumulation of EBS may have been caused by second-generation star-forming activity. The double-peaked features along the sightlines to  $l \sim 70^\circ$  and  $93^\circ$  are caused by significant extinction toward  $l \sim 80^\circ$ , which prevents detections of objects. The Orion Spur happens to be located in this dense region (from a distance of 3 kpc toward  $l \sim 70^\circ$  to 2 kpc toward  $l \sim 93^\circ$ ; for reference, the distance of the equidistant circle in the background image is 5000 light-years or about 1.5 kpc). Similarly rapidly increasing extinction values can also be seen toward  $l \sim 145^\circ$ . Unlike the line of sight toward  $l \sim 80^\circ$ , star-forming activity is not found here.

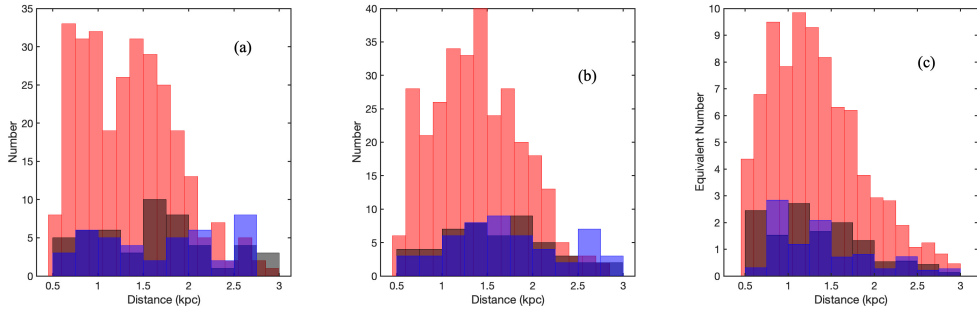


**Figure 6.** Detailed distributions of EBS in different distances along three sightlines. Red, black, and blue bars represent EW-, EB-, and EA-type EBSs, respectively. (a)  $l = 70^\circ$ . (b)  $l = 93^\circ$ . (c)  $l = 150\text{--}210^\circ$ . The equivalent numbers in this latter panel were calculated from a combination of the relevant number density and the area covered, which is the same as for panels (a) and (b) at the same distance ( $N_{\text{equi}} = S_{a,b} \times \frac{N}{S_c}$ ).

In general, the stellar distribution appears inhomogeneous as a function of direction along the Galactic plane. For example, for distances between 0.5 kpc and 3 kpc, compare the sector between  $l \sim 70^\circ$  and  $l \sim 93^\circ$  with a second sector between  $l = 150^\circ$  and  $l = 210^\circ$ : see the bottom panel of Figure 5. The regions contained within the dashed rectangles have widths of 300 pc. The corresponding EBS distributions are shown in Figure 6. Figure 2(e) suggests that our sample’s completeness is higher for systems brighter than  $I = 16$  mag, an upper limit we therefore adopt for our subsequent analysis.

Figure 6a shows that the systems located along this specific sightline ( $l \sim 70^\circ$ ) are distributed inhomogeneously and tend to cluster on scales of several hundred parsecs, irrespective of EBS type. The distribution of EW types exhibits two ridges separated by a valley on a scale of approximately 1 kpc. The EB- and EA-type distributions also show two ridges, within about 2.5 kpc, although the details differ. Within our target sectors, the spatial clustering scale, i.e., the width of the nearby ridges, increases from EW through EB to EA types. Along the same direction, an age gradient can also be discerned. Moreover, the extinction behavior also suggests that these clustering scales reflect reality.

However, the sightline toward  $l \sim 93^\circ$  shows a different pattern, as shown in Figure 6(b). All three types of EBS exhibit clustered distributions between 1 and 2 kpc, but only EA types show a rise beyond 2.5 kpc. Compared with Figure 6(c), which also offers some evidence of clustering behavior, the peak of the distribution along this sightline is located at greater distances. We suspect that the peaked distributions of our EBS may be driven by the structure of the thin disk, as traced by EBS, rather than by sampling incompleteness.

As such, it is clear that the EBS density distribution in the thin disk is not uniform. Future work should address the detailed structure of the Galactic thin disk based on a larger EBS sample.

### 3.3. Absolute parameters

To arrive at homogeneous estimates of the physical parameters of the EW-type EBS in the Galactic plane, we created a model for each system using the 2015 version of the Wilson–Devinney (W–D) code (Wilson & Devinney 1971; Wilson 1979, 1990; Sun et al. 2020). The input parameters of the models were based on the results listed in Table 1. We excluded systems with fewer than 150 photometric epochs given the limited accuracy of the resulting parameters.

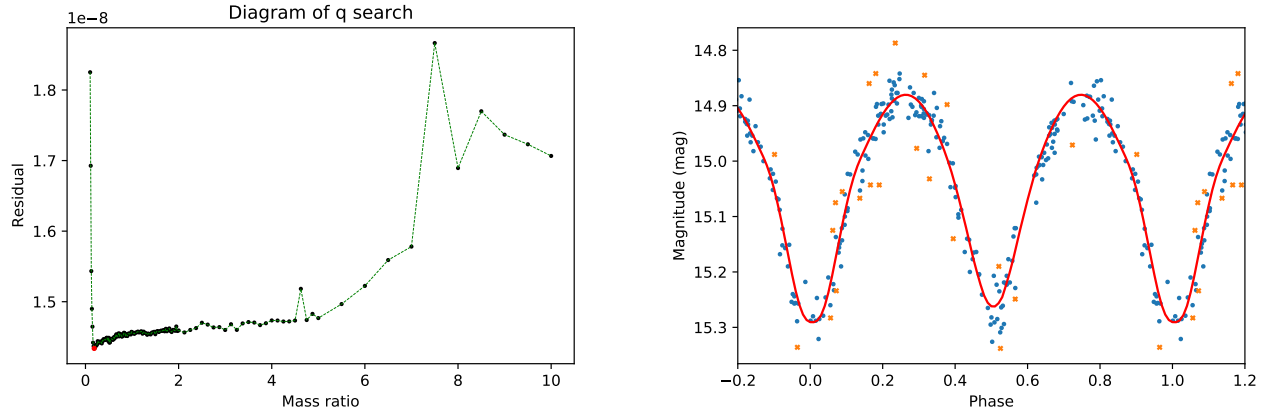


**Figure 7.** Example of our parameter determination procedure. (left) Mass ratio search. The mass ratio associated with minimum residuals was adopted; here  $q = 0.1875$  (shown as a red dot). (right) Best-fitting light curve overplotted on the original observations ( $I$ -band magnitudes). The outliers are marked as orange crosses.

For all systems, ‘Mode 3’ (contact mode, usually applied to systems in geometric contact without constraints on the thermal contact configuration) was used to analyze the light curves. The input light curves were based on the parameters listed in Table 1. The effective temperatures of the primary components were taken from Pecaut & Mamajek (2013), based on their 2MASS ( $J - K_s$ ) colors and the extinction calculated previously. The distances derived from the PLR were used to render absolute system parameters. The bolometric corrections are from Chen et al. (2019).

EW types can be divided into two groups, split at a photospheric temperature of 6200 K (Marsh et al. 2017). The hotter objects correspond to stars dominated by radiative energy transport while cooler objects are stars with convective envelopes. We set the gravity-darkening coefficients and the bolometric albedos to, respectively,  $g = 0.32$  and  $A = 0.5$ , and  $g = 1.0$  and  $A = 1.0$ , for stars with temperatures less and greater than 6200 K, respectively. A bolometric logarithmic limb-darkening law was applied. No spots, third bodies, or time derivatives of the orbital period were considered in our light-curve fitting.

We used an extensive  $q$ -search method to find the best mass ratio,  $q = M_2/M_1$ . Mass ratios  $q$  from 0.1 to 10 were tried, in steps of 0.0125 from 0.1 to 1, 0.025 from 1 to 2, 0.125 from 2 to 5, and 0.5 from 5 to 10; see the left panel of Figure 7. The mass ratios are shown on the horizontal axis, while the residuals are shown on the vertical axis. In this example, the minimum residual occurs for a mass ratio  $q = 0.1875$ . The best-fitting light curve, compared with the original observations, is shown in the right panel of Figure 7. Outliers rejected during our light-curve solution procedures are marked as orange crosses. The phase shift of the primary eclipse, the orbital inclination ( $i$ ), the temperature of the secondary component ( $T_2$ ), the potentials of both components ( $\Omega_1, \Omega_2$ ;  $\Omega_1 = \Omega_2$  in the geometric contact configuration), and the bandpass luminosities of the primary component ( $L_1$ ) were treated as adjustable parameters. To arrive at a more reliable sample, we applied additional selection criteria. We visually checked all best-fitting light curves and excluded those targets that were not well-matched. We did not retain sample objects with inclinations of less than  $50^\circ$ , since the best-fitting parameters for such low inclinations are unreliable.

The results from our light-curve modeling are presented in Table 2. The first column corresponds to the same order as that in Table 1. The input effective temperature of the primary component,  $T_{1o}$ , was determined from its color, and the temperature of the other star,  $T_{2o}$ , was obtained from the best fit. Note that the color index was used to calculate the temperature of the primary star, which may cause a level of bias in the temperatures of both components. We therefore calculated the combined temperature,  $T_{\text{comb}} = \left[ \frac{L_1 + L_2}{L_1/T_{1o}^4 + L_2/T_{2o}^4} \right]^{1/4}$ , where  $T_{1o}, T_{2o}, L_1, L_2$

**Table 2.** EW-type Parameters

ID	$T_1$	$T_2$	$q$	$M_1$	$M_2$	$R_1$	$R_2$	$M_{bol1}$	$M_{bol2}$	$L_1/(L_1 + L_2)$	$\Omega_1 = \Omega_2$	$A$	$i$
	K	K	( $M_2/M_1$ )	$M_\odot$	$M_\odot$	$R_\odot$	$R_\odot$	mag	mag			$R_\odot$	$^\circ$
KISOJ000039.63+622214.1	8157	6551	7.5	0.156	1.167	0.494	1.156	4.78	3.894	0.23	11.821	2.005	57.044
KISOJ000048.17+614603.1	6129	7699	0.462	1.226	0.567	1.042	0.732	3.668	3.475	0.528	2.79	2.304	86.796
KISOJ000053.24+613059.8	4607	4381	4.375	0.251	1.1	0.539	1.041	5.41	4.163	0.248	8.279	2.004	63.157
KISOJ000056.84+625228.4	7337	7698	0.3	1.94	0.582	1.929	1.11	1.567	2.567	0.731	2.463	3.946	56.189
KISOJ000123.66+613746.8	5771	5477	0.4	1.185	0.474	1.246	0.825	3.822	4.926	0.731	2.645	2.647	63.908
KISOJ000208.16+630633.5	5285	5772	0.587	0.963	0.566	0.952	0.746	4.773	4.934	0.548	3.031	2.217	54.22
KISOJ000210.22+611924.2	5312	5588	5.0	0.354	1.768	0.894	1.817	3.662	1.991	0.167	9.015	3.405	58.017
KISOJ000233.43+614514.3	4917	4658	4.375	0.251	1.098	0.605	1.141	5.332	4.17	0.254	8.147	2.154	72.266
KISOJ000250.76+624850.0	5126	5345	4.875	0.213	1.038	0.486	0.977	6.143	4.43	0.174	8.86	1.838	68.057
KISOJ000300.42+631913.6	6261	5215	1.95	0.577	1.125	0.806	1.093	4.013	4.062	0.493	5.137	2.455	83.705
KISOJ000308.44+622223.9	5126	5016	7.5	0.16	1.201	0.48	1.192	5.66	3.762	0.15	12.146	2.132	61.469
KISOJ000329.49+613312.2	5632	5463	1.575	1.01	1.591	1.144	1.396	2.768	2.473	0.425	4.513	3.191	75.15
KISOJ000356.37+611452.6	6356	5651	0.237	2.032	0.483	2.089	1.168	1.355	2.785	0.825	2.216	3.837	67.856
KISOJ000359.11+615018.1	5394	5659	0.188	1.04	0.195	1.13	0.557	4.42	5.783	0.783	2.141	2.052	74.899
KISOJ000401.47+613034.7	4962	5308	0.387	1.115	0.432	1.068	0.692	4.1	4.761	0.65	2.641	2.28	81.237
KISOJ000417.46+620836.4	6733	6526	9.5	0.151	1.438	0.549	1.471	4.978	2.938	0.129	14.35	2.52	66.477
KISOJ000429.77+630856.5	5771	5784	3.25	0.385	1.25	0.834	1.401	4.76	3.579	0.258	6.796	2.807	68.041
KISOJ000441.52+623631.7	6829	6771	1.05	1.838	1.93	2.155	2.197	1.598	1.59	0.496	3.562	5.072	78.901
KISOJ000501.27+611509.9	4729	4840	0.125	1.822	0.228	2.158	0.939	1.854	3.63	0.835	1.958	3.634	71.187
KISOJ000505.12+630032.3	5903	5052	1.3	0.896	1.165	0.915	1.037	3.545	3.9	0.571	4.277	2.621	57.358
...	...	...	...	...	...	...	...	...	...	...	...	...	...

NOTE—This table is available in its entirety in machine-readable form.

are the temperatures and luminosities of both components. Next, the temperatures were corrected by dividing them by  $T_{\text{comb}}/T_{10}$ . A second run was initiated using these new temperatures. The results of the second run,  $T_1$  and  $T_2$ , are the temperatures of the two stars in Table 2. In addition,  $q$  is the best-fitting mass ratio resulting in the smallest residuals, and  $(M_1, M_2, R_1, R_2)$  are the absolute parameters of both stars in units of solar masses and solar radii, where we derived the masses from the mass—luminosity relation (Yildiz & Doğan 2013) and the mass ratio  $q$ .  $M_{\text{bol}1}$  and  $M_{\text{bol}2}$  are the absolute bolometric magnitudes of the primary and secondary stars, respectively.  $\Omega_1 = \Omega_2$  are the potentials of both stars.  $L_1/(L_1 + L_2)$  is the ratio of the bandpass luminosities of the primary star to the total bandpass luminosity, and  $A$  is the length of the semi-major axis, in solar radii, of the relative orbit, which is the sum of the two stars’ absolute semi-major axes,  $A = a_1 + a_2$ ;  $i$ , in the final column, is the binary orbital inclination with respect to the plane of the sky.

We carried out a photometric analysis of all EW-type light curves in the Galactic plane and derived their parameters. This data set will be valuable for further analysis and comparisons with other EW-type EBS.

### 3.4. Cross-check with Gaia

The *Gaia* mission (Gaia Collaboration et al. 2016, 2018, 2020) represents a leap forward for tests of stellar and Galactic astrophysics. In particular, *Gaia* parallaxes, with precisions of  $30\mu\text{as}$  or better for sources with  $G \leq 15$  mag, can be used to solve the greatest and most challenging problems in stellar astrophysics. However, there is clear evidence of the presence of systematic errors in *Gaia* parallaxes. Lindegren et al. (2018) found a general, systematic parallax offset of  $\Delta\pi = 29\mu\text{as}$  from their quasar catalog. The *Gaia* eDR3 parallax solution is a significant improvement compared with that affecting *Gaia* Data Release 2 (DR2): a typical 20% parallax improvement has been reported for *Gaia* eDR3 quasars (Fabricius et al. 2020). However, despite being the best benchmark for *Gaia* parallaxes, quasars (typically with  $G > 17$  mag) are rather faint and their color distribution does not match well the stellar color distribution. Clearly, independent assessment of *Gaia* parallaxes is important to fully characterize any lingering systematic errors. Since EW-type EBS are among the most numerous variables in the Milky Way that have independently determined distance measurements in the solar neighborhood, here we will use our EW-type distances to check for zero-point offsets in the *Gaia* eDR3 parallaxes.

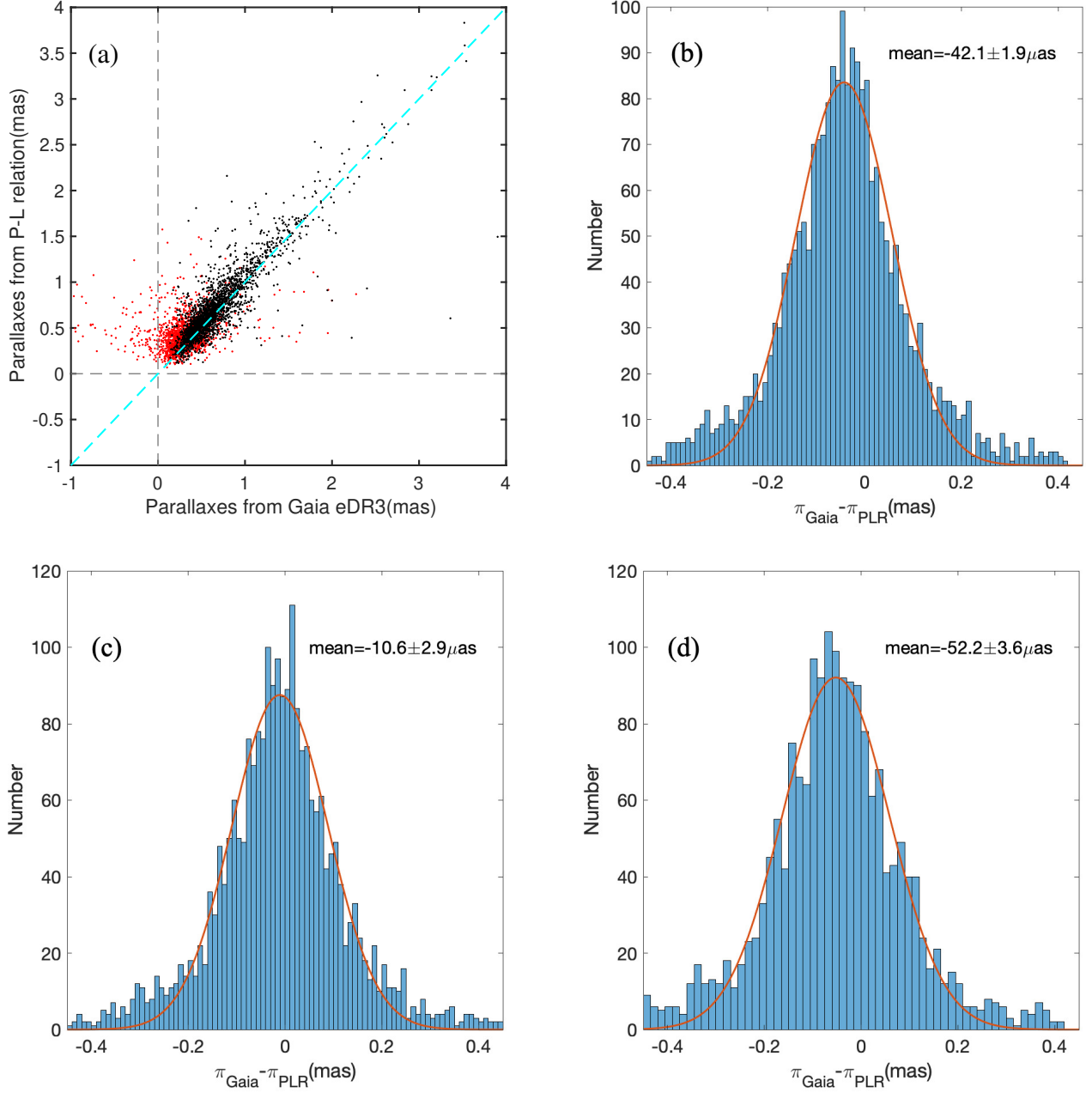


**Figure 8.** Comparison of predicted EBS parallaxes derived from the PLR versus *Gaia* eDR3 parallaxes. (a) Direct comparison for all EW types. Red points have uncertainties exceeding 20% or negative parallaxes. The cyan dashed line is the one-to-one locus. (b) Distribution of the parallax offsets affecting *Gaia* eDR3,  $\Delta\pi(\text{Gaia}_{\text{eDR3}} - \text{PLR}) = -42.1 \pm 1.9 \mu\text{as}$ . (c) Parallax offsets of corrected *Gaia* eDR3 parallaxes (Lindegren et al. 2020),  $\Delta\pi(\text{Gaia}_{\text{eDR3}}^{\text{corr}} - \text{PLR}) = -10.6 \pm 2.9 \mu\text{as}$ . (d) Equivalent distribution of *Gaia* DR2 parallaxes,  $\Delta\pi(\text{Gaia}_{\text{DR2}} - \text{PLR}) = -52.2 \pm 3.6 \mu\text{as}$ . The red curves in panels (b), (c), and (d) represent the best-fitting Gaussian distributions.

Of the 3996 EW-type EBS with distances from the PLR, 3920 have parallaxes available in *Gaia* eDR3. Figure 8(a) shows a direct comparison of the EBS parallaxes derived from the PLR versus *Gaia* eDR3 parallaxes. The cyan dashed one-to-one line is meant to clearly show the extent of the offset in distances. The deviation between the samples hints at a clear offset in parallaxes, in the sense that the PLR parallaxes are larger on average than their *Gaia* counterparts. After excluding objects with large errors and negative parallaxes ( $\sigma_{\pi}/\pi > 0.2$  and  $\pi < 0$ ), marked as red points in Figure 8(a), 2334 EW-type EBS were left. Figure 8(b) presents the distribution of parallax differences,  $\pi_{\text{Gaia}} - \pi_{\text{PLR}}$ .

The distribution appears to be a roughly symmetric, normally distributed offset in the negative direction. The mean offset is  $\Delta\pi = -42.1 \pm 1.9\mu\text{as}$ , where the error is the standard error on the mean for all sample objects. In other words, the *Gaia* parallaxes are systematically smaller.

The *Gaia* team has released a model allowing us to adjust this zero-point offset, which was based on an analysis of quasars, binary stars, and stars in the Large Magellanic Cloud (Lindegren et al. 2020). We also compared the parallaxes implied by our EW-type distances with the corrected *Gaia* parallaxes (see Figure 8c) and found an offset of  $\Delta\pi = -10.9 \pm 2.9\mu\text{as}$ . This suggests that the parallax zero-point correction provided by the *Gaia* team significantly reduces but may not fully eliminate the prevailing bias in the *Gaia* eDR3 parallaxes.

Quantification of the parallax systematics in *Gaia* DR2 was based on careful analysis of a series of tracer objects, yielding: Cepheids,  $\Delta\pi = -46 \pm 13\mu\text{as}$  (Riess et al. 2018); nearby bright EBS,  $\Delta\pi = -82 \pm 33\mu\text{as}$  (Stassun & Torres 2018); stars with asteroseismically determined radii,  $\Delta\pi = -52.8 \pm 2.4\mu\text{as}$  (statistical)  $\pm 8.6\mu\text{as}$  (systematic) (Zinn et al. 2019); and Bayesian distances for a radial velocity sample,  $\Delta\pi = -54 \pm 6.0\mu\text{as}$  (Schönrich et al. 2019)). For comparison, we similarly used our EBS sample as parallax tracer and found  $\Delta\pi = -52.2 \pm 3.6\mu\text{as}$ . This offset is similar to those of other authors' concurrent, independent analyses based on different benchmark samples (e.g., Zinn et al. 2019; Schönrich et al. 2019). Our result should have similar systematic uncertainties as those determined by Zinn et al. (2019) and Schönrich et al. (2019), since the maximum parallax differences among these three tracer populations is less than  $2\mu\text{as}$ .

We will now estimate the likely systematic error range pertaining to our PLR-based EW-type distances. Five fundamental issues affect the level of the systematic uncertainties, including (i) the offset in the PLR, (ii) its internal spread, (iii) uncertainties in the photometric zero points, (iv) errors in our extinction evaluation, and (v) third-component effects.

The PLR was obtained from 183 objects within 330 pc with an average parallax of 5.46 mas. Considering a  $30\mu\text{as}$  systematic uncertainty (Gaia Collaboration et al. 2016), the systematic error contributed by the offset is about 0.5%. The systematic error associated with the internal spread in the PLR is of order  $0.21/\sqrt{183} \approx 0.016$  mag. Here, 0.21 mag is the mean spread in the  $IJK_s$ -band PLRs. As regards the photometric zero points, the  $I$ -band systematic error is most important, given that the  $JHK_s$ -band PLR and KISOGP EW data both came from 2MASS; our  $I$ -band photometric data for all EBS PLRs was based on the USNO-B catalog. We correlated our  $I$ -band data for all sample EBS with that published in the USNO-B catalog. We found that the KISOGP  $I$ -band magnitudes are systematically 0.009 mag brighter than the corresponding USNO-B  $I$ -band magnitudes for the 6894 targets in common.

Since we make use of the  $IJK_s$  bands, here we consider an average extinction corresponding to  $0.225A_V$ . We also adopt a 10% uncertainty in the extinction determination, which reflects uncertainties owing to the choice of extinction law. For a mean observed extinction of  $A_V = 1.94\text{mag}$ , these choices lead to an uncertainty of  $1.94\text{mag} \times 0.225 \times 10\% = 0.0437$  mag. Next, if a third component can be discerned, a study of 75 nearby EW-type EBS (D'Angelo et al. 2006) has shown that this will affect the systematic uncertainty at the median distance of our sample by about 0.3%. As neither our KISOGP sample objects nor those contributing to the PLR explicitly excluded third-body effects, the bias caused by third- or higher-order multiplicity should not differ much between both sets of EBS. We estimate that the associated systematic uncertainty is less than 0.3%. As such, the systematic uncertainty range affecting our results is  $\sigma = 581\mu\text{as} \times [(0.005)^2 + (0.016 \times \ln(10)/5)^2 + (0.009 \times \ln(10)/5)^2 + (0.0437 \times \ln(10)/5)^2 + (0.003)^2]^{1/2} = 12.9\mu\text{as}$ .

The offset we found based on our catalog of 2334 EW-type EBS is well within the prevailing uncertainties and also fully consistent with a systematic error below  $100\mu\text{as}$  as reported by the *Gaia* team. Our EW-type EBS in the Galactic plane result in a larger offset than that derived from quasars ( $-17\mu\text{as}$ ), but the offset can be reduced significantly by application of the official parallax zero-point correction. The *Gaia* team found that the parallax zero-point depends on a target's magnitude, color, and position, and hence the small difference we found between EBS and quasars is not surprising. The difference may come from the details of the distribution of the parallax zero-point, since quasars are fainter and bluer than our EBS, which are all located in the Galactic plane. In addition, for faint sources outside the Galactic disk parallax calibrations are estimated directly from the quasar sample. However, the parallax bias for objects in the Milky Way is derived indirectly, based on binary stars and stars in the Large Magellanic Cloud.

Stassun & Torres (2021) found a mean parallax offset of  $-37 \pm 20\mu\text{as}$ , which decreased to  $-15 \pm 18\mu\text{as}$  following the official corrections based on 76 EBS. Their result matches our result well, which is particularly encouraging since our result is affected by small statistical errors and based on a large sample. Our EBS sample can be used as useful tracers for further work on the zero-point offset of *Gaia* parallaxes. In addition, our result is based on EW-type EBS in the Galactic plane, which most other studies try to avoid. It can therefore serve as a useful reference for other

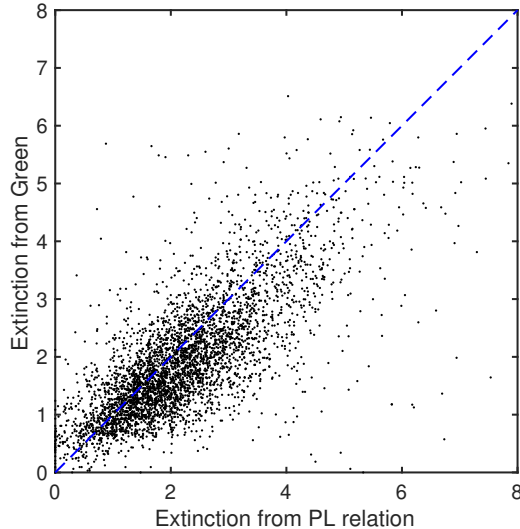


**Figure 9.** Extinction comparison ( $A_V$ , mag) between the values derived from the PLR and from Green et al. (2019).

studies that need to deal with the *Gaia* zero-point offset in the Galactic plane and complement studies of the zero-point distribution across the sky.

In conclusion, we found a *Gaia* eDR3 zero-point offset of  $\Delta\pi = -42.1 \pm 1.9$  (stat.)  $\pm 12.9$  (syst.)  $\mu\text{as}$ , based on 2334 EW-type EBS covering a wide range of magnitudes and extinction values in the northern Galactic plane. The official parallax zero-point correction can significantly reduce the bias in eDR3 parallaxes to  $-10.9 \pm 2.9$  (stat.)  $\pm 12.9$  (syst.)  $\mu\text{as}$  (for our sample).

### 3.5. Extinction compared with 3D extinction map

Green et al. (2019) presented a three-dimensional (3D) dust reddening map of the northern sky derived from *Gaia* parallaxes and stellar photometry from Pan-STARRS 1 and 2MASS. Green et al.’s 3D extinction map happens to overlap with the KISOGP survey’s spatial coverage. In Figure 9, we compare the extinction derived from our PLR analysis with that from the 3D extinction map.

As shown in Figure 9, a linear correlation is clearly discernible. The extinction values from both studies fit well within the relevant scatter envelopes. This scatter may originate from various sources. First, the error in the extinction from both our PLR analysis and that in the 3D extinction map cannot be ignored. Second, the error in distance used as input into the 3D extinction map may exacerbate the intrinsic errors in the extinction from the 3D map. Finally, the distances and spatial resolutions pertaining to the 3D map are coarse, with distance modulus steps of 0.5 mag and angular resolutions of several arcminutes. These steps lead to non-negligible errors when comparing the extinction values for single objects, particularly for our sample in the Galactic plane where the extinction is usually high. In any case, given the prevailing uncertainties, both methods are mutually consistent.

## 4. CONCLUSION

We have presented a new catalog of EBS in the northern Galactic plane based on the KISOGP survey. We visually identified 7055 EBS spread across  $\sim 330$  deg<sup>2</sup>, including 4197 EW-, 1458 EB-, and 1400 EA-type EBS. For all sample objects, we used their *I*-band light curves to determine accurate parameters, including their periods (accurate to better than the fifth decimal place), a reference  $t_0$ , the depths of the two eclipses, etc.

We also examined the spatial distribution of our sample objects. We found an inhomogeneous density distribution of EBS in the thin disk at different Galactic longitudes. In addition, we found a random distribution of the ratios of the eclipse depths for EA types and a concentration tending to unity for EW-type EBS. Moreover, we checked that the distributions of their periods vary among different EBS types, increasing from EW to EB and EA type. We also obtained the distribution of the eclipse depths, the *I*-band magnitudes, etc. Finally, we tested the level of contamination of our sample by other types of variables, which we found to be negligible.

We derived the distances and extinction values pertaining to the EW types in our sample using their PLRs, reaching distances in excess of 6 kpc and  $V$ -band extinction values exceeding  $A_V = 9$  mag. We combined our EBS sample with HMSFRs and Cepheids to trace the structure of the thin disk. Stars of the same type (including but not limited to EBS) tend to cluster on spatial scales of several hundred parsecs. Using different tracers, we revealed some structural properties of the thin disk.

As an independent distance measurement, our EBS distance analysis offers a complementary measurement of the global parallax offset affecting *Gaia* eDR3. We found  $\Delta\pi = -42.1 \pm 1.9$  (stat.)  $\pm 12.9$  (syst.)  $\mu\text{as}$  based on a careful analysis of 2334 EW-type EBS. Our newly derived offset is consistent with the results from the *Gaia* team. We also found that the official parallax zero-point correction can significantly reduce the bias affecting the eDR3 parallaxes. Finally, we performed a photometric analysis of all EW-type light curves using the W–D method to derive individual system parameters, and we cross checked our extinction values with Green et al.’s 3D extinction map.

We acknowledge long-term support for the KISOGP project from the staff at Kiso Observatory, Japan. We are grateful for research support from the National Key Research and Development Program of China through grants 2019YFA0405500 and 2017YFA0402702. This work was also partially supported by the National Natural Science Foundation of China (NSFC) through grant 11973001. N. M. acknowledges financial support from Grants-in-Aid (Nos. 26287028 and 18H01248) from the Japan Society for the Promotion of Science. X. C. acknowledges support from NSFC grant 11903045.

## REFERENCES

- Akerlof, C., Amrose, S., Balsano, R., et al. 2000, *AJ*, **119**, 1901
- Alonso-García, J., Dékány, I., Catelan, M., et al. 2015, *AJ*, **149**, 99
- Chen, X., de Grijs, R., & Deng, L. 2016, *ApJ*, **832**, 138
- Chen, X., Deng, L., de Grijs, R., et al. 2018a, *ApJ*, **859**, 140
- Chen, X., Wang, S., Deng, L., et al. 2018b, *ApJS*, **237**, 28
- . 2020, *ApJS*, **249**, 18
- Chen, Y., Girardi, L., Fu, X., et al. 2019, *A&A*, **632**, A105
- Clarke, D. 2002, *A&A*, **386**, 763
- Cook, K. H., Alcock, C., Allsman, H. A., et al. 1995, *IAU Colloq.*, **155**, 221
- D’Angelo, C., van Kerkwijk, M. H., & Rucinski, S. M. 2006, *AJ*, **132**, 650
- Drake, A. J., Graham, M. J., Djorgovski, S. G., et al. 2014, *ApJS*, **213**, 9
- Drake, A. J., Djorgovski, S. G., Catelan, M., et al. 2017, *MNRAS*, **469**, 3688
- Eggen, O. J. 1967, *MmRAS*, **70**, 111
- Fabricius, C., Luri, X., Arenou, F., et al. 2020, *arXiv*, [arXiv:2012.06242](https://arxiv.org/abs/2012.06242)
- Gaia Collaboration, Brown, A. G. A., Vallenari, A., et al. 2020, *arXiv*, [arXiv:2012.01533](https://arxiv.org/abs/2012.01533)
- . 2016, *A&A*, **595**, A2
- . 2018, *A&A*, **616**, A1
- Genovali, K., Lemasle, B., Bono, G., et al. 2014, *A&A*, **566**, A37
- Graczyk, D., Soszyński, I., Poleski, R., et al. 2011, *AcA*, **61**, 103
- Green, G. M., Schlafly, E., Zucker, C., et al. 2019, *ApJ*, **887**, 93
- Haas, M., Hackstein, M., Ramolla, M., et al. 2012, *Astron. Nachr.*, **333**, 706
- Heinze, A. N., Tonry, J. L., Denneau, L., et al. 2018, *AJ*, **156**, 241
- Hempel, M., Minniti, D., Dékány, I., et al. 2014, *The Messenger*, **155**, 24
- Hoffman, D. I., Harrison, T. E., Coughlin, J. L., et al. 2008, *AJ*, **136**, 1067
- Hoffman, D. I., Harrison, T. E., & McNamara, B. J. 2009, *AJ*, **138**, 466
- Jayasinghe, T., Kochanek, C. S., Stanek, K. Z., et al. 2018, *MNRAS*, **477**, 3145
- Jetsu, L., Porceddu, S., Lyytinen, J., et al. 2013, *ApJ*, **773**, 1
- Kochanek, C. S., Shappee, B. J., Stanek, K. Z., et al. 2017, *PASP*, **129**, 104502
- Lafler, J., & Kinman, T. D. 1965, *ApJS*, **11**, 216
- Lindgren, L., Hernández, J., Bombrun, A., et al. 2018, *A&A*, **616**, A2
- Lindgren, L., Bastian, U., Biermann, M., et al. 2020, *arXiv*, [arXiv:2012.01742](https://arxiv.org/abs/2012.01742)
- Lomb, N. R. 1976, *Ap&SS*, **39**, 447
- Lucy, L. B. 1968a, *ApJ*, **151**, 1123
- . 1968b, *ApJ*, **153**, 877



- Madore, B. F., Freedman, W. L., & Moak, S. 2017, *ApJ*, **842**, 42
- Marsh, F. M., Prince, T. A., Mahabal, A. A., et al. 2017, *MNRAS*, **465**, 4678
- Mateo, N. M., & Rucinski, S. M. 2017, *AJ*, **154**, 125
- Matsunaga, N. 2017, *Eur. Phys. J.*, **152**, 01027
- Matsunaga, N., Bono, G., Chen, X., et al. 2018, *SSRv*, **214**, 74
- Minniti, D., Lucas, P. W., Emerson, J. P., et al. 2010, *NewA*, **15**, 433
- Paczyński, B., Szczygieł, D. M., Pilecki, B., & Pojmański, G. 2006, *MNRAS*, **368**, 1311
- Palaversa, L., Ivezić, Ž., Eyer, L., et al. 2013, *AJ*, **146**, 101
- Pawlak, M., Graczyk, D., Soszyński, I., et al. 2013, *AcA*, **63**, 323
- Pawlak, M., Soszyński, I., Udalski, A., et al. 2016, *AcA*, **66**, 421
- Pecaut, M. J., & Mamajek, E. E. 2013, *ApJS*, **208**, 9
- Pietrukowicz, P., Mróz, P., Soszyński, I., et al. 2013, *AcA*, **63**, 115
- Pojmanski, G. 1997, *AcA*, **47**, 467
- Reid, M. J., Menten, K. M., Brunthaler, A., et al. 2014, *ApJ*, **783**, 130
- Riess, A. G., Casertano, S., Yuan, W., et al. 2018, *ApJ*, **861**, 126
- Rucinski, S. M. 1994, *PASP*, **106**, 462
- . 2006, *MNRAS*, **368**, 1319
- Rucinski, S. M., & Duerbeck, H. W. 1997, *PASP*, **109**, 1340
- Rygl, K. L. J., Brunthaler, A., Sanna, A., et al. 2012, *A&A*, **539**, A79
- Scargle, J. D. 1982, *ApJ*, **263**, 835
- Schönrich, R., McMillan, P., & Eyer, L. 2019, *MNRAS*, **487**, 3568
- Skrutskie, M. F., Cutri, R. M., Stiening, R., et al. 2006, *AJ*, **131**, 1163
- Sokolovsky, K. V., Gavras, P., Karamelas, A., et al. 2017, *MNRAS*, **464**, 274
- Soszyński, I., Stepień, K., Pilecki, B., et al. 2015, *AcA*, **65**, 39
- Soszyński, I., Pawlak, M., Pietrukowicz, P., et al. 2016, *AcA*, **66**, 405
- Stassun, K. G., & Torres, G. 2018, *ApJ*, **862**, 61
- . 2021, *arXiv*, [arXiv:2101.03425](https://arxiv.org/abs/2101.03425)
- Stepień, K. 2006a, *AcA*, **56**, 199
- . 2006b, *AcA*, **56**, 347
- . 2009, *MNRAS*, **397**, 857
- . 2011, *AcA*, **61**, 139
- Sun, W., Chen, X., Deng, L., & de Grijs, R. 2020, *ApJS*, **247**, 50
- Torres, G., Andersen, J., & Giménez, A. 2010, *A&A Rv*, **18**, 67
- Wang, S., & Chen, X. 2019, *ApJ*, **877**, 116
- Wang, S., Jiang, B. W., Zhao, H., et al. 2017, *ApJ*, **848**, 106
- Wilson, R. E. 1979, *ApJ*, **234**, 1054
- . 1990, *ApJ*, **356**, 613
- Wilson, R. E., & Devinney, E. J. 1971, *ApJ*, **166**, 605
- Woźniak, P. R., Williams, S. J., Vestrand, W. T., & Gupta, V. 2004, *AJ*, **128**, 2965
- Yao, Y., Liu, C., Deng, L., et al. 2017, *ApJS*, **232**, 16
- Yildiz, M., & Doğan, T. 2013, *MNRAS*, **430**, 2029
- Zinn, J. C., Pinsonneault, M. H., Huber, D., & Stello, D. 2019, *ApJ*, **878**, 136